Orbital frustration and topological flat bands

Wenjuan Zhang,* Zachariah Addison,* and Nandini Trivedi
Department of Physics, Ohio State University, Columbus, Ohio 43210, USA

(Received 19 July 2021; revised 1 November 2021; accepted 2 November 2021; published 9 December 2021)

We expand the concept of frustration in Mott insulators and quantum spin liquids to metals with flat bands. We show that when *inter*orbital hopping t_2 dominates over *intra*orbital hopping t_1, in a multiband system with strong spin-orbit coupling λ, electronic states with a narrow bandwidth $\Delta \sim (t_2)^2/\lambda$ are formed compared to a bandwidth of order t_1 for intraorbital hopping dominated models. We demonstrate the evolution of the electronic structure, Berry phase distributions for time-reversal and inversion breaking cases, and their imprint on the optical absorption in a tight-binding model of d-orbital hopping on a honeycomb lattice. Going beyond quantum Hall effects and twisted bilayer graphene, we provide an alternative mechanism and a richer materials' platform for achieving flat bands poised at the brink of instabilities toward novel correlated and fractionalized metallic phases.

DOI: 10.1103/PhysRevB.104.235202

I. INTRODUCTION

Symmetry and topology have played a fundamental role in characterizing emergent phases in quantum matter. From the well-understood emergence of long-range order in crystals, magnets, and superconductors, research has moved to the frontiers of a new type of truly exotic order, namely topological order, in which the quantum numbers of the excitations are fractionalized. A key ingredient to obtain fractionalization is frustration of the motion of the electron that leads to a small kinetic energy and hence to flat bands in the electronic spectrum. Our main goal is to provide a design principle for creating materials in which the interorbital hopping t_2 dominates over intraorbital hopping t_1, in a multiband system with strong spin-orbit coupling λ, that generates electronic states with a narrow bandwidth $\Delta \sim (t_2)^2/\lambda$ compared to a bandwidth of order t_1 for intraorbital dominated hopping models. We expect these designer flat-band materials to provide a link between frustrated metals and frustrated magnetic insulators, paving the way for the search and discovery of topologically ordered states.

Emergent phases in quantum matter are understood today under two paradigms: the Landau paradigm, which has been the pillar for phases arising from the spontaneous breaking of symmetry, and the topological paradigm, in which phases are characterized by topological invariants leading to quantized response functions. Within the topological paradigm, there are broadly two classes: phases where interactions are less important, such as the integer quantum Hall effect, topological insulators [1,2], Weyl semimetals [3,4], and topological superconductors [5,6]; and the more exotic class, where interactions dominate along with topology, yielding a new type of order, dubbed topological order [7–9]. These include two candidates so far: (i) the fractional quantum Hall effect (FQHE) [10–13] in a two-dimensional electron gas subjected to a large magnetic field in which charge is fractionalized, and (ii) quantum spin liquids in Mott insulators in which spin is fractionalized [14–16].

Fractionalization in the FQHE arises because the kinetic energy is quenched and the bands become completely flat in a high magnetic field upon projecting to the lowest Landau level [see Fig. 1(a)], and consequently, the relatively strong electron-electron Coulomb interactions open a bulk gap in the metallic regime with edge states that carry the signature of fractional charge in quantized Hall and quantized thermal Hall transport. Further, quantum spin liquids emerge in Mott insulators due to magnetic frustration [17–27]. In the celebrated Kitaev magnets with bond-dependent frustrating interactions, for example, spins are fractionalized into Majorana modes that have recently been shown to produce a quantized thermal Hall conductance in a candidate material α-$RuCl_3$ [16,28–31].

Recently, the community has seen feverish activity in twisted bilayer graphene in which flat bands emerge when the angle of mismatch is a very specific *magic* angle of around 1° yielding a large-scale moiré pattern with lattice constant a_M much larger than that of a graphene sheet a_G [32,33] [see Fig. 1(b)]. For the most ideal *magic* angles, the flat bands are separated from other dispersing bands by an energy gap $\delta \sim 10$ meV leading to a flatness ratio of $\mathcal{F} = \Delta/\delta \lesssim 0.5$ [34,35]. The flat bands have resulted in the observation of strongly correlated superconducting and Mott insulating phases [36–42]; however, so far fractionalized metallic states have not been observed.

In this paper, we demonstrate a mechanism for achieving flat bands in *metallic* systems with strong spin-orbit coupling λ. The basic mechanism involves frustrating the motion of an electron by suppressing intraorbital hopping t_1 compared to hopping between different orbitals t_2. We dub this mechanism, which leads to small bandwidths of order $(t_2)^2/\lambda$ and small flatness ratios $\mathcal{F} \sim (t_2/\lambda)^2$, *spin-orbit assisted interorbital frustration* [see Fig. 1(c)]. Importantly, these flatbands have

*These authors contributed equally.

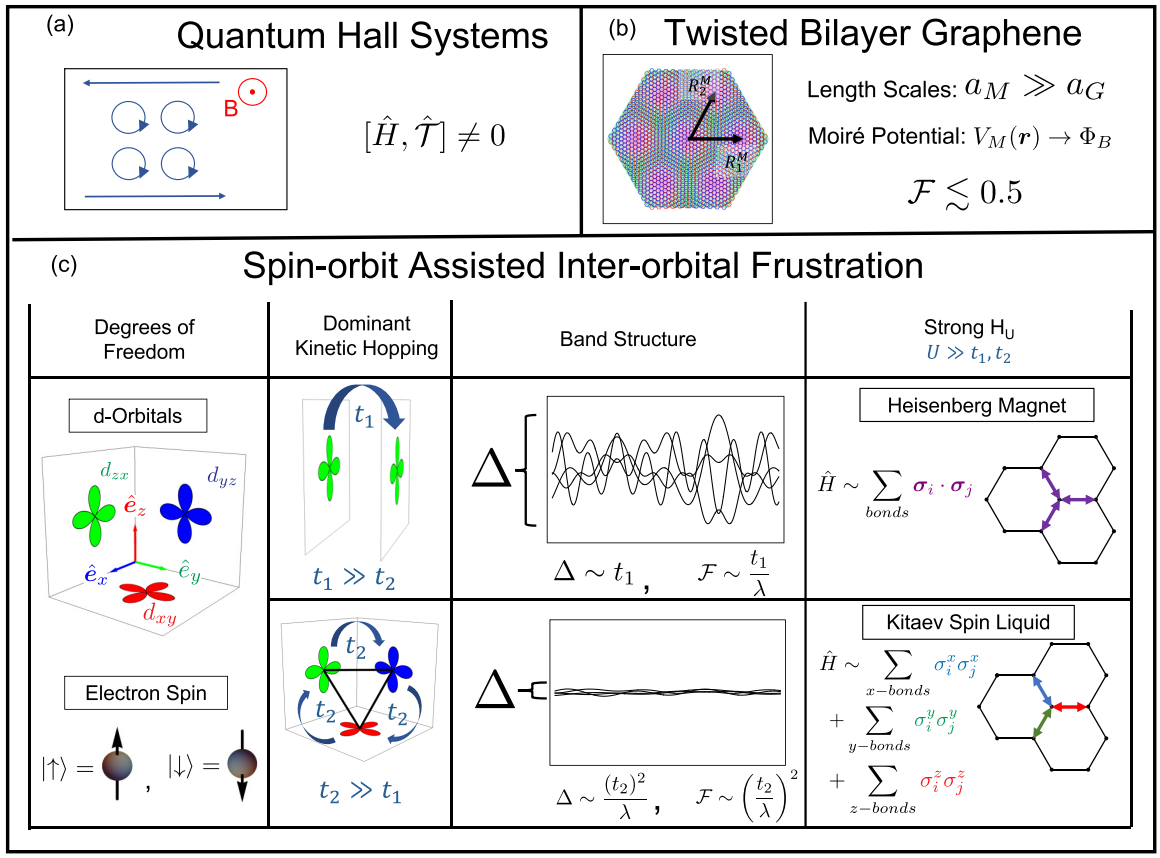

FIG. 1. Three mechanisms for generating flat bands: (a) by localizing electrons in a large magnetic field $\boldsymbol{B}$ in two dimensions in quantum Hall systems; (b) from a periodic interlayer moiré potential $V_M(\boldsymbol{r})$ in "magic-angle" twisted bilayer graphene with period $a_M \gg a_G$, the graphene lattice constant, yielding a flatness ratio of $\mathcal{F} \lesssim 0.5$. (c) Our proposal of achieving flat bands via spin-orbit interaction λ assisted interorbital frustration whereby dominant interorbital hopping t_2 in an effective $j = 1/2$ multiplet on the honeycomb lattice leads to a flatness ratio $\mathcal{F} \sim (t_2/\lambda)^2$. The strong interacting limit of dominant intraorbital t_1 or dominant interorbital t_2 hopping leads to Heisenberg or an Kitaev Hamiltonian, respectively (see Sec. III).

nontrivial momentum space Berry phase distributions that encode the mixing of the orbital degrees of freedom on the lattice and that influence the anomalous Hall conductivity and the dynamical conductivity.

We choose the parameters of our tight-binding Hamiltonian to ensure that with on-site Hubbard interactions, in the strong-coupling limit, we obtain the Kitaev model with bond-dependent interactions, and we contrast it with the parameters that generate the isotropic Heisenberg model. We show that in the metallic itinerant phase, the presence of strong spin-orbit interactions, λ, can lead to frustration whereby the kinetic energy of a multiplet of bands is suppressed in systems where intersite interorbital hopping, t_2, dominates over intersite intraorbital hopping t_1. We calculate the electrical conductivity in two regimes: systems dominated by t_2 and systems dominated by t_1, for which we show the crossover and consequences of the momentum space Berry phase distributions in the frustrated flat band phase.

II. MODEL

We consider a honeycomb lattice of transition-metal ions surrounded by the octahedral cages formed by the ligands. The ions' d-orbitals split into a threefold t_{2g} sector and a twofold degenerate e_g sector separated by the crystal field δ_{CF} energy. In the low-energy t_{2g} sector, the general tight-binding Hamiltonian on a honeycomb lattice can be written as

$$\hat{H} = \sum_{\langle ij\rangle,\alpha\beta,\sigma} t_{ij}^{\alpha\beta} \hat{d}_{\alpha\sigma}^{\dagger}(\boldsymbol{r}_i)\hat{d}_{\beta\sigma}(\boldsymbol{r}_j) + \sum_{i,\alpha\beta,\sigma\sigma'} \lambda_{\sigma\sigma'}^{\alpha\beta} \hat{d}_{\alpha\sigma}^{\dagger}(\boldsymbol{r}_i)\hat{d}_{\beta\sigma'}(\boldsymbol{r}_i), \tag{1}$$

where $\hat{d}_{\alpha\sigma}^{\dagger}(\boldsymbol{r}_i)$ and $\hat{d}_{\alpha\sigma}(\boldsymbol{r}_i)$ are the fermionic annihilation and creation operators at site $\boldsymbol{r}_i$ for orbital α and spin σ.

The honeycomb lattice can be described by a primitive triangular lattice with two sites A and B per unit cell. Each A and B site has three nearest-neighboring sites. We orient the honeycomb such that the primitive lattice vectors can be chosen to be $\boldsymbol{R}_1 = a\sqrt{3}/2\hat{\boldsymbol{x}} + a/2\hat{\boldsymbol{y}}$ and $\boldsymbol{R}_2 = a\sqrt{3}/2\hat{\boldsymbol{x}} - a/2\hat{\boldsymbol{y}}$, where a is the lattice constant. We denote the three vectors connecting an A site to its nearest-neighboring B sites as $\boldsymbol{v}_x = -a/2\sqrt{3}\hat{\boldsymbol{x}} + a/2\hat{\boldsymbol{y}}$, $\boldsymbol{v}_y = -a/2\sqrt{3}\hat{\boldsymbol{x}} - a/2\hat{\boldsymbol{y}}$, and $\boldsymbol{v}_z = a/\sqrt{3}\hat{\boldsymbol{x}}$. and we also define a set of bond axes $\hat{\boldsymbol{\gamma}}_x = -1/\sqrt{6}\hat{\boldsymbol{x}} + 1/\sqrt{2}\hat{\boldsymbol{y}} + 1/\sqrt{3}\hat{\boldsymbol{z}}$, $\hat{\boldsymbol{\gamma}}_y = -1/\sqrt{6}\hat{\boldsymbol{x}} - 1/\sqrt{2}\hat{\boldsymbol{y}} + 1/\sqrt{3}\hat{\boldsymbol{z}}$, and $\hat{\boldsymbol{\gamma}}_z = \sqrt{2/3}\hat{\boldsymbol{x}} + 1/\sqrt{3}\hat{\boldsymbol{z}}$ whose projection onto the plane of the honeycomb is in the direction of nearest-neighbor bond vectors $\boldsymbol{v}_s$ [see Fig. 2(d)].

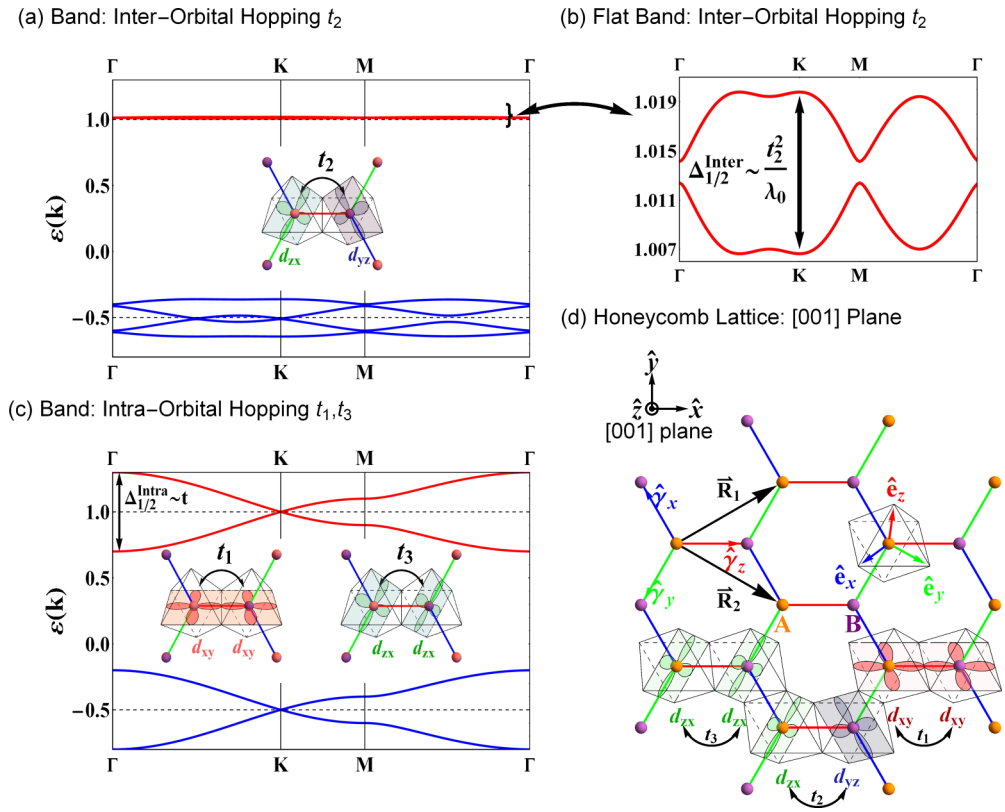

FIG. 2. Band structures with spin-orbit coupling λ_0 on a honeycomb lattice: (a) Bands $\varepsilon(\boldsymbol{k})$, in units of λ_0, for dominant interorbital hopping $t_2 = 0.1\lambda_0$ and intraorbital hopping $t_1 = t_3 = 0$. The bandwidth of the upper $j = 1/2$ multiplet $\Delta_{1/2}^{\text{inter}} \sim t^2/\lambda_0 \sim 0.01\lambda_0$. (b) Inset highlighting the flat bands in the upper $j = 1/2$ manifold of (a). (c) Bands of intraorbital dominated hopping $t_1 = t_3 = 0.1\lambda_0$ and $t_2 = 0$. The bandwidth of the upper $j = 1/2$ multiplet is $\Delta_{1/2}^{\text{intra}} \sim t_1 \sim 0.1\lambda_0$. (d) Honeycomb lattice in the [001] plane showing orthogonal Cartesian axes $(\hat{\boldsymbol{x}}, \hat{\boldsymbol{y}}, \hat{\boldsymbol{z}})$, bond axes $(\hat{\boldsymbol{\gamma}}_x, \hat{\boldsymbol{\gamma}}_y, \hat{\boldsymbol{\gamma}}_z)$, and orbital axes $(\hat{\boldsymbol{e}}_x, \hat{\boldsymbol{e}}_y, \hat{\boldsymbol{e}}_z)$, and intersite intraorbital and intersite interorbital processes.

The tight-binding model in Eq. (1) is the sum of two terms: a kinetic part describing the overlap between nearest-neighboring d-orbitals on the honeycomb lattice, and a spin-orbit part describing the on-site interaction between the spin and orbital degrees of freedom of the t_{2g} sector. It is easiest to write these couplings in a maximally symmetric coordinate system whereby the d-orbitals $|d_\alpha(\boldsymbol{r}_i)\rangle$ and spin are defined with respect to the orthogonal orbital unit vectors $\hat{\boldsymbol{e}}_x = -1/\sqrt{2}\hat{\boldsymbol{x}} - 1/\sqrt{6}\hat{\boldsymbol{y}} + 1/\sqrt{3}\hat{\boldsymbol{z}}$, $\hat{\boldsymbol{e}}_y = 1/\sqrt{2}\hat{\boldsymbol{x}} - 1/\sqrt{6}\hat{\boldsymbol{y}} + 1/\sqrt{3}\hat{\boldsymbol{z}}$, and $\hat{\boldsymbol{e}}_z = \sqrt{2/3}\hat{\boldsymbol{y}} + 1/\sqrt{3}\hat{\boldsymbol{z}}$, which are related to the bond axes by a $\pi/2$ counterclockwise rotation. In this basis, the nearest-neighbor kinetic interactions can be written in terms of matrices $T_{\gamma(\boldsymbol{r}_i,\boldsymbol{r}_j)}$, where $\gamma(\boldsymbol{r}_i, \boldsymbol{r}_j)$ takes three values $\gamma(\boldsymbol{r}_i, \boldsymbol{r}_j) = x, y, z$ corresponding to the vector $\boldsymbol{v}_s$ that connects nearest-neighbor sites $\boldsymbol{r}_i$ and $\boldsymbol{r}_j$. We write the symmetry-allowed components of these matrices

$$t_{ij}^{\alpha\beta}\delta_{\sigma\sigma'} = T_{\gamma(\boldsymbol{r}_i,\boldsymbol{r}_j)}^{\alpha\beta}\delta_{\sigma\sigma'} = \langle d_{\alpha\sigma}(\boldsymbol{r}_i)|\,\hat{t}\,|d_{\beta\sigma'}(\boldsymbol{r}_j)\rangle \tag{2}$$

in the basis of orbitals $\{|d_{yz}(\boldsymbol{r}_i)\rangle, |d_{zx}(\boldsymbol{r}_i)\rangle, |d_{xy}(\boldsymbol{r}_i)\rangle\}$ defined with respect to the axes $\hat{\boldsymbol{e}}_i$ as

$$T_x = \begin{bmatrix} t_3 & 0 & 0 \\ 0 & t_1 & t_2 \\ 0 & t_2 & t_1 \end{bmatrix}, \quad T_y = \begin{bmatrix} t_1 & 0 & t_2 \\ 0 & t_3 & 0 \\ t_2 & 0 & t_1 \end{bmatrix},$$

$$T_z = \begin{bmatrix} t_1 & t_2 & 0 \\ t_2 & t_1 & 0 \\ 0 & 0 & t_3 \end{bmatrix}. \tag{3}$$

Symmetry constrains the nearest-neighbor hopping matrices to have three independent parameters t_1, t_2, and t_3. The intersite interorbital coupling is described by t_2, while t_1 and t_3 describe the intersite intraorbital couplings.

The second term in Eq. (1) describes the on-site spin-orbit interaction $\lambda_{\sigma\sigma'}^{\alpha\beta}\delta_{ij} = \langle d_{\alpha\sigma}(\boldsymbol{r}_i)|\,\hat{\lambda}\,|d_{\beta\sigma'}(\boldsymbol{r}_j)\rangle$ between the d-orbitals in the t_{2g} sector: $\hat{\lambda} = \frac{2\lambda_0}{\hbar^2}\sum_i \hat{L}_{\hat{\boldsymbol{e}}_i} \otimes \hat{S}_{\hat{\boldsymbol{e}}_i}$. Here $\hat{S}_{\hat{\boldsymbol{e}}_i} = (\hbar/2)\hat{\sigma}_{\hat{\boldsymbol{e}}_i}$, and $\hat{\sigma}_{\hat{\boldsymbol{e}}_i}$ is the Pauli matrix in the $\hat{\boldsymbol{e}}_i$ direction. The angular momentum operators can be expressed in terms of matrices $L_{\boldsymbol{e}_i}$ whose components $L_{\boldsymbol{e}_i}^{\alpha\beta}\delta_{\sigma\sigma'}\delta_{\boldsymbol{r}_i\boldsymbol{r}_j} = \langle d_{\alpha\sigma}(\boldsymbol{r}_i)|\,\hat{L}_{\hat{\boldsymbol{e}}_i}\,|d_{\beta\sigma'}(\boldsymbol{r}_j)\rangle$ in the orbital basis are

$$L_{\boldsymbol{e}_x} = \begin{bmatrix} 0 & 0 & 0 \\ 0 & 0 & -i \\ 0 & i & 0 \end{bmatrix}, \quad L_{\boldsymbol{e}_y} = \begin{bmatrix} 0 & 0 & i \\ 0 & 0 & 0 \\ -i & 0 & 0 \end{bmatrix},$$

$$L_{\boldsymbol{e}_z} = \begin{bmatrix} 0 & -i & 0 \\ i & 0 & 0 \\ 0 & 0 & 0 \end{bmatrix}. \tag{4}$$

In the absence of $\hat{t}$, the spin-orbit interactions split the t_{2g} sector into states of total angular momentum $j = 1/2$ and $3/2$ separated by an energy $3/2\lambda_0$.

III. STRONG-COUPLING EXPANSION

Upon adding a strong on-site multiorbital Hubbard interaction to Eq. (1) of the form

$$\hat{H}_U = \sum_i \left(\frac{U - 3J_H}{2}(\hat{n}_i - 1)^2 - 2J_H \hat{\boldsymbol{S}}_i \cdot \hat{\boldsymbol{S}}_i - \frac{J_H}{2}\hat{\boldsymbol{L}}_i \cdot \hat{\boldsymbol{L}}_i \right), \tag{5}$$

where $\hat{n}(\boldsymbol{r}_i)$, $\hat{\boldsymbol{S}}(\boldsymbol{r}_i)$, and $\hat{\boldsymbol{L}}(\boldsymbol{r}_i)$ are the density, spin, and orbital angular momentum operator at site $\boldsymbol{r}_i$, in the limit of strong spin-orbit coupling $\lambda \gg t$ and strong Hubbard interactions an expansion in powers of t leads to an effective $\mathcal{J}$-K-Γ Hamiltonian for a system where half of the $j = 1/2$ multiplet is filled, given by

$$\hat{H}_{\text{eff}} = \sum_{\langle i,j \rangle} \Bigg(\mathcal{J}\hat{\boldsymbol{J}}(\boldsymbol{r}_i) \cdot \hat{\boldsymbol{J}}(\boldsymbol{r}_j) + K\hat{J}_{\hat{\boldsymbol{e}}_\gamma}(\boldsymbol{r}_i)\hat{J}_{\hat{\boldsymbol{e}}_\gamma}(\boldsymbol{r}_j) + \sum_{\alpha\beta} \Gamma(\hat{J}_{\hat{\boldsymbol{e}}_\alpha}(\boldsymbol{r}_i)\hat{J}_{\hat{\boldsymbol{e}}_\beta}(\boldsymbol{r}_j) + \hat{J}_{\hat{\boldsymbol{e}}_\beta}(\boldsymbol{r}_i)\hat{J}_{\hat{\boldsymbol{e}}_\alpha}(\boldsymbol{r}_j)) \Bigg). \tag{6}$$

Here $\gamma \to \gamma(\boldsymbol{r}_i, \boldsymbol{r}_j)$ is an implicit function of the lattice sites, $\boldsymbol{r}_i$ and $\boldsymbol{r}_j$, and $\hat{\boldsymbol{J}}_i$ is the total angular momentum operator projected onto the $j = 1/2$ state space,

$$\hat{\boldsymbol{J}} = \sum_{m=\pm 1/2} |1/2, m_j\rangle \langle 1/2, m_j| (\hat{\boldsymbol{S}} + \hat{\boldsymbol{L}}) |1/2, m_j\rangle \langle 1/2, m_j| . \tag{7}$$

The coupling strengths $\mathcal{J}$, K, and Γ in the limit $t_i << \lambda << U$ are given by [43,44]

$$\begin{aligned} \mathcal{J} &= \frac{4}{27}\left(\frac{6t_1(t_1 + 2t_3)}{U - 3J_H} + \frac{2(t_1 - t_3)^2}{U - J_H} + \frac{(2t_1 + t_3)^2}{U + 2J_H} \right), \\ K &= \frac{8J_H}{9}\left(\frac{(t_1 - t_3)^2 - 3t_2^2}{(U - 3J_H)(U - J_H)} \right), \\ \Gamma &= \frac{16J_H}{9}\left(\frac{t_2(t_1 - t_3)}{(U - 3J_H)(U - J_H)} \right). \end{aligned} \tag{8}$$

We see that in the limit of purely intraorbital hopping ($t_2 = 0$) and $t_1 = t_3$ but nonzero, the effective Hamiltonian is that of a Heisenberg magnet ($K = \Gamma = 0$), while in the limit of purely interorbital hopping ($t_2 \neq 0$) and $t_1 = t_3 = 0$ the effective Hamiltonian is purely Kitaev type with $\mathcal{J} = \Gamma = 0$. In this model, the interorbital coupling t_2 acts as an effective *spin*-orbit interaction where the orbital degrees of freedom take the role of an effective *spin*. In the limit $t_1 = t_3 = 0$, this effective interaction gives rise to a pseudospin frustration that leads to the effective Kitaev-type interaction in Eq. (6). The alternative limit $t_i \ll U \ll \lambda$ is less studied and may be a promising avenue to engineer other types of spin-liquid phases. Here we focus on the itinerant metallic phase where in the absence of interactions and for $t_i \ll \lambda$ flat bands emerge in the presence of dominant intersite interorbital hopping.

IV. FLAT BANDS

By using the discrete translation symmetry of the system, the Hamiltonian in Eq. (1) yields a 12×12 matrix [$(2j + 1) \times 2$ atoms], the Bloch Hamiltonian, $\hat{H}(\boldsymbol{k})$, whose components can be written as $H_{\chi\gamma}(\boldsymbol{k}) = \sum_{\boldsymbol{\Delta}} H_{\chi\gamma}(\boldsymbol{\Delta}, \boldsymbol{\delta}) e^{-i\boldsymbol{\Delta}\cdot\boldsymbol{k}} e^{-i\boldsymbol{\delta}\cdot\boldsymbol{k}}$ with $H_{\chi\xi}(\boldsymbol{R}_i - \boldsymbol{R}_j, \boldsymbol{\tau}_i - \boldsymbol{\tau}_j) = \langle d_\chi(\boldsymbol{R}_i + \boldsymbol{\tau}_i)| \hat{H} |d_\xi(\boldsymbol{R}_j + \boldsymbol{\tau}_j)\rangle$. Here χ and ξ index the spin, orbital, and sublattice degrees of freedom of the localized atomic states on the lattice. In this basis, the Bloch Hamiltonian can be written as

$$\hat{H}(\boldsymbol{k}) = \sum_{\mu,\alpha} t_{\mu\alpha}(\boldsymbol{k})(\Gamma_\mu \otimes \mathcal{D}_\alpha \otimes \mathbb{1}) + \sum_i \lambda_0(\mathbb{1} \otimes L_{\hat{\boldsymbol{e}}_i} \otimes S_{\hat{\boldsymbol{e}}_i}), \tag{9}$$

where Γ_μ are the two-dimensional Pauli matrices describing the A/B sublattice degrees of freedom, $\mathbb{1}$ is the two-dimensional identity matrix, and $t_{\mu\alpha}(\boldsymbol{k})$ is the three-dimensional matrices $\mathcal{D}_\alpha$ that satisfy

$$\begin{aligned} \sum_\alpha t_{x\alpha}(\boldsymbol{k})\mathcal{D}_\alpha &= \text{Re}\left(\sum_i e^{i\boldsymbol{k}\cdot\boldsymbol{v}_i} T_i \right), \\ \sum_\alpha t_{y\alpha}(\boldsymbol{k})\mathcal{D}_\alpha &= \text{Im}\left(\sum_i e^{i\boldsymbol{k}\cdot\boldsymbol{v}_i} T_i \right), \\ t_{z\alpha}(\boldsymbol{k}) &= 0, \end{aligned} \tag{10}$$

where $\boldsymbol{v}_i$ are the three vectors defined above that connect an A site to its neighboring B sites.

We now investigate the eigenvalues of the Bloch Hamiltonian in the purely intraorbital ($t_2 = 0$, $t_1 = t_3 \neq 0$) and interorbital ($t_2 \neq 0$, $t_1 = t_3 = 0$) kinetic limits. For general orbital hopping, our model satisfies time-reversal symmetry ($\hat{\mathcal{T}} = i\sigma_{\hat{\boldsymbol{e}}_y} K$) and inversion symmetry ($\hat{\mathcal{I}} = \Gamma_x$) endowed by the honeycomb lattice structure ($[\hat{\mathcal{T}}, \hat{H}] = [\hat{\mathcal{I}}, \hat{H}] = 0$). These symmetries result in a Kramers degeneracy throughout the Brillouin zone such that bands must be at least twofold-degenerate for all crystal momenta $\boldsymbol{k}$ independent of the value of the kinetic hopping parameters t_1, t_2, and t_3. In the absence of t_i, the coupling between neighboring sites on the lattice vanishes and the Hamiltonian consists of completely local interactions that describe flat bands separated into two manifolds: a manifold with total angular momentum $j = 1/2$ containing four bands, and a manifold with total angular momentum $j = 3/2$ containing eight bands. This multiplet structure $(4 + 8)$ remains for $\lambda \gg t$, though j is no longer a good quantum number.

Figures 2(a) and 2(c) show the band structure along high-symmetry directions in the Brillouin zone for hopping parameters in the extreme intraorbital and interorbital kinetic limits. In the intraorbital dominated limit, the absence of interorbital hopping ($t_2 = 0$) results in an additional interorbital symmetry such that each band in the $j = 3/2$ sector is fourfold-degenerate throughout the Brillouin zone, while the $j = 1/2$ sector contains two twofold-degenerate bands protected by time-reversal and inversion symmetry. Band touching points occur at the $\boldsymbol{K} = (2\pi/\sqrt{3}a, 2\pi/3a)$ and $\boldsymbol{K}' = (2\pi/\sqrt{3}a, -2\pi/3a)$ points in the Brillouin zone. This results in an eightfold-degenerate double Dirac point for the $j = 3/2$ sector and fourfold-degenerate Dirac points for the $j = 1/2$

TABLE I. Eigenvalues of $W^{3/2}_{\alpha\beta}(\boldsymbol{k})$ at high-symmetry points in the Brillouin zone in the intraorbital and interorbital dominated kinetic limits. Eigenvalues are given in units of the nonzero kinetic coupling t. Each eigenvalue is twofold-degenerate due to time-reversal and inversion symmetry.

Intraorbital Dominated Interactions	Eigenvalues $[t_1]$			
Γ	$9/2$	$3/2$	$-3/2$	$-9/2$
K/K'	0	0	0	0
M	$3/2$	$1/2$	$-1/2$	$-3/2$
Interorbital Dominated Interactions	**Eigenvalues $[t_2]$**			
Γ	$\sqrt{1+\sqrt{7/16}}$	$\sqrt{1-\sqrt{7/16}}$	$-\sqrt{1-\sqrt{7/16}}$	$-\sqrt{1+\sqrt{7/16}}$
K/K'	$\sqrt{2-\sqrt{15/16}}$	0	0	$-\sqrt{2-\sqrt{15/16}}$
M	$\sqrt{1+\sqrt{7/16}}$	$\sqrt{1-\sqrt{7/16}}$	$-\sqrt{1-\sqrt{7/16}}$	$-\sqrt{1+\sqrt{7/16}}$

sector. Note that neither of these topological degeneracies is protected by crystalline symmetries. They can be converted to manifolds containing just twofold-degenerate bands through the introduction of other symmetry-allowed interorbital interactions, and they are simply an artifact of the finely tuned nature of the purely intraorbital coupling limit.

In the limit of extreme interorbital kinetics, intraorbital interactions are turned off ($t_1 = t_3 = 0$) and the orbital interactions are dominated by the interorbital coupling t_2. The $j = 3/2$ multiplet is split into four twofold-degenerate bands, while the $j = 1/2$ multiplet consists of two twofold-degenerate bands with almost no dispersion. The intraband kinetic energy is quenched due to an interorbital-spin-orbit frustration caused by the large on-site spin-orbit interaction λ_0 and nonzero t_2 that leads to the appearance of flat bands.

To understand how these flat bands emerge in the presence of nonzero $\hat{t}$, we use degenerate perturbation theory to calculate the energy splitting of the spin-orbit split bands in orders of the kinetic hopping coefficients t_1, t_2, and t_3. Remarkably for purely interorbital hopping, the first-order correction to the energy bands of the $j = 1/2$ manifold vanishes. This is due to the orbital character of the $j = 1/2$ manifold and the orbital character of the purely interorbital hopping matrices. The action of these matrices on the $j = 1/2$ manifold transforms a $j = 1/2$ state into a mixture of $j = 3/2$ states. These states are all orthogonal to the $j = 1/2$ manifold as they have different eigenvalues with respect to $\hat{\lambda}$. To find the band splitting, we must then go to second-order perturbation theory leading to an effective bandwidth in the purely interorbital hopping limit $\Delta^{\text{inter}}_{1/2} \sim (t_2)^2/\lambda$. This is in contrast to the band splitting of the $j = 3/2$ manifold of states and of either multiplet in the purely intraorbital hopping limit where the first-order correction to the spin-orbit split flat bands is nonzero. In these cases, the action of the kinetic hopping, $\hat{t}$, transforms a state with eigenvalue $j = 1/2$ or $3/2$ into a linear combination of $j = 1/2$ and $3/2$ states, leading to a bandwidth $\Delta \sim t$.

These results are most easily determined by writing the Bloch Hamiltonian in the basis of total angular momentum eigenstates $j = 1/2, 3/2$. In this basis, the Hamiltonian takes the form

$$\hat{H}(\boldsymbol{k}) = \begin{pmatrix} \lambda_0 \mathbb{1}_{4\times 4} + \boldsymbol{\mathcal{M}}^{1/2}_k(t_1,t_3) & \boldsymbol{G}_k(t_1,t_2,t_3) \\ \boldsymbol{G}^{\dagger}_k(t_1,t_2,t_3) & -\frac{\lambda_0}{2}\mathbb{1}_{8\times 8} + \boldsymbol{\mathcal{M}}^{3/2}_k(t_1,t_2,t_3) \end{pmatrix}, \tag{11}$$

where $\boldsymbol{\mathcal{M}}^{1/2}_k(t_1,t_3)$ is a 4×4 matrix, $\boldsymbol{\mathcal{M}}^{3/2}_k(t_1,t_2,t_3)$ is an 8×8 matrix, and $\boldsymbol{G}_k(t_1,t_2,t_3)$ is a 4×8 matrix that are all linear functions of the kinetic couplings t_i. We see that $\boldsymbol{\mathcal{M}}^{1/2}_k(t_1,t_3)$ is independent of the interorbital kinetic coupling t_2 and thus vanishes in the purely interorbital hopping limit $t_1 = t_3 = 0$, while the other matrices remain nonzero. This forces the linear-in-t perturbations to the eigenvalues of the $j = 1/2$ manifold in the upper-left 4×4 block of $\hat{H}(\boldsymbol{k})$ to vanish, while in this limit the lower-right 8×8 block $\boldsymbol{\mathcal{M}}_{3/2}(t_1,t_2,t_3)$ is nonvanishing and leads to the order-t perturbation to the eigenvalues of the $j = 3/2$ sector being nonzero. In contrast for the purely intraorbital hopping limit, the matrices $\boldsymbol{\mathcal{M}}^{1/2}_k(t_1,t_3)$, $\boldsymbol{\mathcal{M}}^{3/2}_k(t_1,t_2,t_3)$, and $\boldsymbol{G}_k(t_1,t_2,t_3)$ are all nonzero, leading to nonzero first-order perturbations to the spin-orbit split flat bands.

In the absence of $\hat{t}$, the Hamiltonian in Eq. (1) consists of a band structure of flat band multiplets of total angular momentum $j = 1/2$ and $3/2$. To calculate the energy splitting of the degenerate $j = 1/2$ and $3/2$ multiplets to linear order in $\hat{t}$, we use degenerate perturbation theory and first calculate the components of the matrix

$$W^{j}_{\alpha\beta}(\boldsymbol{k}) = \left\langle \psi^{j}_{\alpha} \right| \sum_{\mu,\gamma} t_{\mu\gamma}(\boldsymbol{k})(\Gamma_\mu \otimes \mathcal{D}_\gamma \otimes \mathbb{1}) \left| \psi^{j}_{\beta} \right\rangle, \tag{12}$$

where $|\psi^{j}_{\alpha}\rangle$ are the eigenstates of $\hat{\lambda}$ with total angular momentum j. The eigenvalues of the matrix $W^{j}_{\alpha\beta}(\boldsymbol{k})$ are the first-order corrections to the eigenvalues of $\hat{\lambda}$ [45].

For the $j = 3/2$ manifold, the eigenvalues of $W^{3/2}_{\alpha\beta}(\boldsymbol{k})$ are nonzero and complicated functions of $\boldsymbol{k}$. Table I lists eigenvalues of $W^{3/2}_{\alpha\beta}(\boldsymbol{k})$ at some high-symmetry momenta in the Brillouin zone for the intraorbital and interorbital dominated kinetic limits. Each eigenvalue is doubly degenerate because of Kramers theorem and the presence of time-reversal and

inversion symmetries. We also note the vanishing of the first-order correction to the band energies at the $\boldsymbol{K}$ and $\boldsymbol{K}'$ momenta in the intraorbital dominated coupling limit. This is reflected in the full band structure by the presence of the eightfold-degenerate double Dirac point contained in the $j = 3/2$ manifold as plotted in Fig. 2(c). To maintain this multifold degeneracy, higher-order corrections to the band dispersion at these points must vanish. Lastly, we note that the first-order correction to the band energies predicts a bandwidth $\Delta_{3/2}$ of the $j = 3/2$ manifold that is of order the hopping strength ($\Delta \sim t$) for both the intraorbital and interorbital dominated kinetic limits.

This is in striking contrast to the $j = 1/2$ manifold of states where $W^{1/2}_{\alpha\beta}(\boldsymbol{k})$ is nonzero in the intraorbital dominated coupling limit, but vanishes in the interorbital dominated limit. For general kinetic hopping t, its eigenvalues are

$$\delta E^{(1)}_{\pm}(\boldsymbol{k}) = \pm\frac{2t_1 + t_3}{3}\sqrt{3 + 4\cos\left(\frac{\sqrt{3}}{2}k_x a\right)\cos\left(\frac{1}{2}k_y a\right) + 2\cos\left(k_y a\right)}, \tag{13}$$

where each eigenvalue $\delta E_{\pm}(\boldsymbol{k})$ is again twofold-degenerate because of Kramers' theorem. In both the intraorbital and interorbital dominated coupling limit, $\delta E_{\pm}(\boldsymbol{K}) = \delta E_{\pm}(\boldsymbol{K}') = 0$. In the intraorbital dominated limit ($t_2 = 0$), this results in the presence of Dirac cones at the $\boldsymbol{K}$ and $\boldsymbol{K}'$ points in the Brillouin zone [see Fig. 2(c)] as further higher-order corrections to the band structure also vanish at these high-symmetry points. Remarkably in the interorbital dominated kinetic limit, $t_1 = t_3 = 0$, $W^{1/2}_{\alpha\beta} = 0$. This is due to the orbital character of the $j = 1/2$ manifold and the orbital character of the purely interorbital hopping matrices. The action of these matrices on the $j = 1/2$ manifold transforms a $j = 1/2$ state into a mixture of $j = 3/2$ states. These states are all orthogonal to the $j = 1/2$ manifold as they have different eigenvalues with respect to $\hat{\lambda}$ forcing $W^{1/2}_{\alpha\beta}(\boldsymbol{k})$ to vanish. This demonstrates that the first-order correction to the energy eigenvalues vanishes in the $j = 1/2$ manifold and for the extreme interorbital dominated limit.

To calculate any nonzero dispersion in this limit and in the $j = 1/2$ manifold, we must proceed to second-order degenerate perturbation theory. However, the calculation is simplified in the interorbital dominated limit due to $W^{1/2}_{\alpha\beta}(\boldsymbol{k}) = 0$. The second-order correction to the $j = 1/2$ manifold of bands is given by

$$\delta E^{(2)}_{\alpha}(\boldsymbol{k}) = \sum_{\beta}\frac{\left\langle\psi^{1/2}_{\alpha}\right|\hat{t}(\boldsymbol{k})\left|\psi^{3/2}_{\beta}\right\rangle\left\langle\psi^{3/2}_{\beta}\right|\hat{t}(\boldsymbol{k})\left|\psi^{1/2}_{\alpha}\right\rangle}{E^{(0)}_{1/2} - E^{(0)}_{3/2}}, \tag{14}$$

where $E^{(0)}_{1/2}$ and $E^{(0)}_{3/2}$ are eigenvalues of $\hat{\lambda}$ for the $j = 1/2$ and $3/2$ manifold, and where

$$\hat{t}(\boldsymbol{k}) = \sum_{\mu,\alpha} t_{\mu\alpha}(\boldsymbol{k})(\Gamma_{\mu} \otimes \mathcal{D}_{\alpha} \otimes \mathbb{1}). \tag{15}$$

The difference $E^{(0)}_{1/2} - E^{(0)}_{3/2} = 3/2\lambda_0$ is of order the spin-orbit coupling λ_0, while the numerator will be of order t_2 squared. We see that this leads to a bandwidth in the $j = 1/2$ manifold and in the interorbital dominated limit of $\Delta^{\text{inter}}_{1/2} \sim (t_2)^2/\lambda_0$, whereas the bandwidths in the purely intraorbital hopping limit $\Delta^{\text{intra}}_{1/2}$ and the bandwidth of the $j = 3/2$ manifold in either limit are all of order t.

In the presence of nonzero intraorbital hopping, the first-order kinetic correction to the spin-orbit split bands is of order t_1 and t_3. In the limit $t_1, t_3 \ll (t_2)^2/\lambda_0$, the dispersion of the eigenenergies of the full Bloch Hamiltonian is proportional to the interorbital hopping t_2 and inversely proportional to the on-site spin-orbit scale λ_0, and it leads to bandwidths in the $J = 1/2$ multiplet of states $\Delta_{1/2} \sim (t_2)^2/\lambda_0$ similar to the completely frustrated limit ($t_1 = t_3 = 0$), while in the limit $(t_2)^2/\lambda_0 \lesssim t_1, t_3$ the dominant intraorbital dynamics diminishes orbital frustration and leads to bandwidths in the $J = 1/2$ multiplet $\Delta_{1/2} \sim t_1, t_3$.

Thus the ingredients for achieving *spin-orbit assisted interorbital frustration* that leads to flat bands in the $j = 1/2$ manifold in the interorbital dominated limit are the vanishing of the first-order perturbative correction to the band energies deriving from the orbital character of the $j = 1/2$ manifold of states and the orbital character of a purely interorbital coupling between sites, and the presence of a large spin-orbit interaction for which the $j = 1/2$ and $3/2$ manifolds are separated by a large energy gap and for which t_2/λ_0 is small.

V. QUANTUM BAND GEOMETRY AND SYMMETRY BREAKING

The quantum geometry of a band structure is determined by a band's Berry potential $\boldsymbol{A}_n(\boldsymbol{k}) = i\langle u_n(\boldsymbol{k})|\nabla_k|u_n(\boldsymbol{k})\rangle$ and curvature $\boldsymbol{\Omega}_n(\boldsymbol{k}) = \nabla_k \times \boldsymbol{A}_n(\boldsymbol{k})$, whose integral across the 2D Brillouin zone dictates the winding of the phase of the Bloch wave function: an integer topological invariant called the Chern number. In the purely atomic limit, whereby the hopping of electrons across lattice sites is strictly forbidden, the Berry curvature is trivially zero. Here we show that in the presence of strong intersite interorbital interactions, t_2, the orbital structure of Bloch eigenstates becomes strongly mixed across the Brillouin zone leading to unique Berry curvature density in the presence of time-reversal and inversion breaking perturbations.

The Berry curvature is a pseudovector such that for inversion symmetric systems $\boldsymbol{\Omega}^k_n(-\boldsymbol{k}) = \boldsymbol{\Omega}^k_n(\boldsymbol{k})$, and for time-reversal symmetric systems $\boldsymbol{\Omega}^k_n(-\boldsymbol{k}) = -\boldsymbol{\Omega}^k_n(\boldsymbol{k})$. In the models described above, time-reversal and inversion symmetry constrain the Berry curvature to vanish in every band n and at all crystal momentum $\boldsymbol{k}$, so $\boldsymbol{\Omega}_n(\boldsymbol{k}) = 0\ \forall \boldsymbol{k}, \forall n$.

To observe nonzero Berry curvature, we perturb our model system with a time-reversal breaking perturbation that couples directly to the electronic spin or with an inversion breaking on-site sublattice potential,

$$\hat{H}'_{\mathcal{T}} = \sum_{i,\sigma\sigma',\alpha}\mu_B \boldsymbol{B}_0 \cdot \boldsymbol{\sigma}_{\sigma\sigma'}\hat{d}^{\dagger}_{\alpha\sigma}(\boldsymbol{r}_i)\hat{d}_{\alpha\sigma'}(\boldsymbol{r}_i), \tag{16}$$

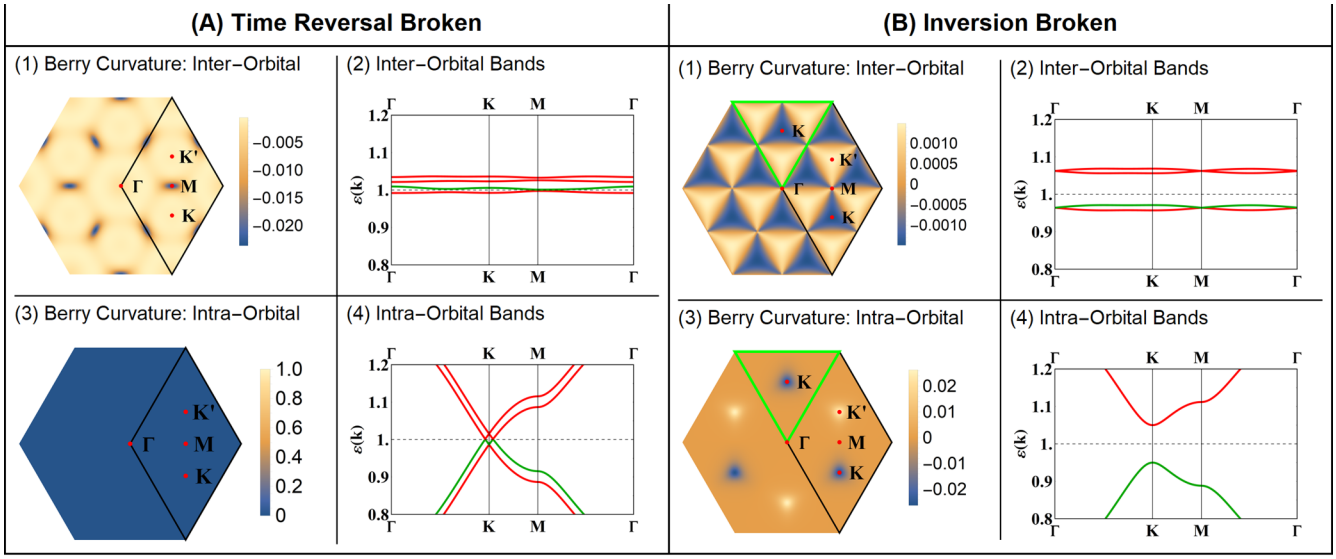

FIG. 3. Berry curvature distribution (in units of a^2) for [panels (a)] time-reversal broken Hamiltonian ($\mu_B|\mathbf{B}_0| = 0.05\lambda_0$) and [panels (b)] for inversion broken Hamiltonian ($|m_0| = 0.05\lambda_0$): (1) Berry curvature of 10th band; (2) band structure of 9th to 12th bands in the purely interorbital hopping limit ($t_2 = 0.1\lambda_0, t_1 = t_3 = 0$); (3) Berry curvature of 10th band; (4) band structure of 9th to 12th bands for purely intraorbital limit ($t_1 = t_3 = 0.1\lambda_0, t_2 = 0$). The regions outlined in green in panel (b), parts (1) and (3), show the fractionalization of the Berry curvature distribution around the $\boldsymbol{K}$ and $\boldsymbol{K}'$ points in the Brillouin zone as one interpolates between the purely intraorbital and purely interorbital hopping limits.

$$\hat{H}'_{\mathcal{I}} = \sum_{i,\sigma,\alpha} m_0(\boldsymbol{r}_i)\hat{d}^{\dagger}_{\alpha\sigma}(\boldsymbol{r}_i)\hat{d}_{\alpha\sigma}(\boldsymbol{r}_i), \tag{17}$$

where $m_0(\boldsymbol{r}_i) = +1\,(-1)$ if site $\boldsymbol{r}_i$ is in the $A\,(B)$ sublattice. Figure 3 shows the band structure and Berry curvature for the second lowest band in the $j = 1/2$ multiplet in the intraorbital and interorbital hopping dominated limits.

When time reversal is broken, bands in the $j = 1/2$ manifold are split in both the purely intraorbital and purely interorbital hopping limits. In the intraorbital limit, internal orbital symmetry allows bands to cross near the $\boldsymbol{K}$ and $\boldsymbol{K}'$ points in the Brillouin zone. In this case, the Berry curvature vanishes everywhere except at the points where bands cross and the curvature becomes ill-defined. In the interorbital dominated limit, peaks in the Berry curvature occur near the $\boldsymbol{M}$ points in the Brillouin zone where the band gap between the lowest and second lowest bands of the $j = 1/2$ multiplet becomes narrow.

When inversion symmetry is broken, in the intraorbital limit, internal orbital symmetry allows bands in the $j = 1/2$ manifold to remain twofold-degenerate at every point in the Brillouin zone. The single-band Berry curvature is ill-defined in the presence of degenerate bands, and thus for these inversion broken systems we plot the Berry phase density for a state with chemical potential filling half the $j = 1/2$ multiplet. We first partition the Brillouin zone into small plaquettes and compute the Berry flux through each plaquette,

$$\phi(\boldsymbol{k}) = -\mathrm{Im}(\mathrm{Ln}(\det(\boldsymbol{\mathcal{U}}))), \tag{18}$$

where $\boldsymbol{\mathcal{U}}_{nm} = \langle u_n(\boldsymbol{k}_N)|u_m(\boldsymbol{k}_0)\rangle$, with n and m taking values over all bands up to the half-filled $j = 1/2$ multiplet, and where the state $|u_n(\boldsymbol{k}_N)\rangle$ is calculated by parallel transport of the state $|u_n(\boldsymbol{k}_0)\rangle$ from $\boldsymbol{k_0}$ around a plaquette centered at $\boldsymbol{k}$ [46]. The Berry curvature is then found by dividing $\phi(\boldsymbol{k})$ by the area of the plaquette. We find that the Berry curvature is localized at the $\boldsymbol{K}$ and $\boldsymbol{K}'$ points where the band gap between the lower and upper bands of the $j = 1/2$ multiplet narrows. In the inversion broken interorbital hopping dominated limit, the narrow bands in the $j = 1/2$ multiplet are split everywhere except at the $\boldsymbol{\Gamma}$ and $\boldsymbol{M}$ points, where the bands come together and form two twofold-degenerate points and the Berry curvature is ill-defined. Away from these points, the Berry curvature disperses in a threefold symmetric pattern with its saddle points along high-symmetry lines connecting the $\boldsymbol{\Gamma}$ and $\boldsymbol{M}$ points in the Brillouin zone.

VI. OPTICAL SIGNATURES

The topological and geometric character of the band structures of the purely intraorbital hopping and interorbital hopping limits can be distinguished in the system's response to a frequency-dependent electric field. To understand the optical response of our model to external frequency-dependent electric field perturbations, we calculate the optical conductivity tensor. The conductivity tensor $\sigma_{ij}(t, t') \in \mathcal{R}$ such that $\sigma_{ij}(-\omega) = \sigma^*_{ij}(\omega)$. Furthermore, time-reversal symmetry constrains the antisymmetric part of the conductivity to vanish, $\sigma_{ij}(\omega) = \sigma_{ji}(\omega)$ [47,48]. Crystalline threefold rotational symmetry about a lattice point constrains the diagonal parts of the conductivity to be equal [$\sigma(\omega) = \sigma_{xx}(\omega) = \sigma_{yy}(\omega)$] while in-plane twofold rotational symmetry constrains $\sigma_{xy}(\omega) = \sigma_{yx}(\omega) = 0$ [49].

The optical conductivity has two contributions. The intraband contribution, $\sigma_F(\omega)$, derives from electromagnetic induced transitions on the Fermi surface. Here we focus on systems where there are 10 electrons per unit cell such that the $j = 3/2$ multiplet is completely filled and the $j = 1/2$

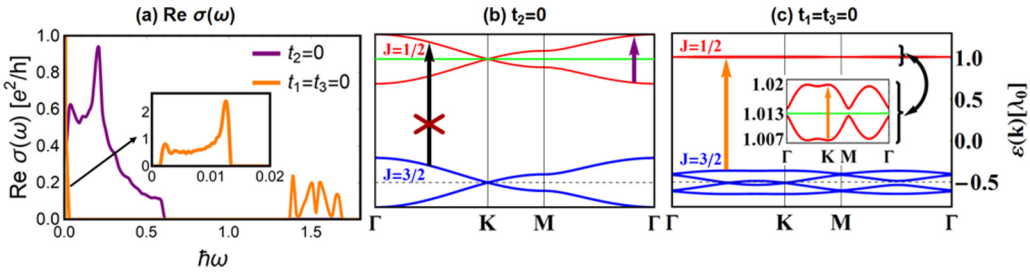

FIG. 4. (a) $\mathrm{Re}(\sigma(\omega))$ for system in the purely interorbital (orange) $t_2 = 0.1\lambda_0$; $t_1 = t_3 = 0$ and purely intraorbital (purple) $t_1, t_3 = 0.1\lambda_0$; $t_2 = 0$ hopping limits, with the chemical potential [shown in green in (b)] set in the middle of the $j = 1/2$ multiplet (with $\hbar\omega$ in units of λ_0). Selection rules for the purely intraorbital hopping limit, and (c) for the purely interorbital hopping limit. Allowed transitions are depicted by colored arrows, whose contribution to the conductivity are shown in (a).

multiplet is half-filled. In the intraorbital dominated coupling limit, the system is a semimetal whose Fermi surface contains just two crystal momenta at the $\boldsymbol{K}$ and $\boldsymbol{K}'$ points in the Brillouin zone. At these points in the band structure, the energy states of the $j = 1/2$ multiplet come together resulting in two fourfold-degenerate points whose low-energy effective theory resembles that of two half-filled Dirac cones. In the interorbital dominated limit, the system is insulating and the band-gap minimum has moved away from the $\boldsymbol{K}$ and $\boldsymbol{K}'$ points to the $\boldsymbol{\Gamma}$ and $\boldsymbol{M}$ points. In both cases, the Fermi surface is of vanishing measure, leading to a negligible intraband contribution to the conductivity at zero temperature.

The second contribution to the conductivity, $\sigma_I(\omega)$, derives from optically induced interband transitions between occupied and unoccupied Bloch states with the same crystal momentum $\boldsymbol{k}$. Here we focus on calculating the real symmetric part of the interband optical conductivity, $\mathrm{Re}(\sigma_I(\omega))$, that couples to real optical transitions between Bloch states whose energy differs by ω [50,51].

The absorption, the real symmetric part of the interband conductivity, can be written as

$$\mathrm{Re}(\sigma_I(\omega)) = \frac{e^2\pi\hbar}{V}\sum_{nm\boldsymbol{k}} \frac{f_n^T(\boldsymbol{k},\mu) - f_m^T(\boldsymbol{k},\mu)}{\varepsilon_n(\boldsymbol{k}) - \varepsilon_m(\boldsymbol{k})} \times \mathrm{Re}(v^x_{nm}(\boldsymbol{k})v^x_{mn}(\boldsymbol{k}))\delta(\varepsilon_n(\boldsymbol{k}) - \varepsilon_m(\boldsymbol{k}) + \hbar\omega). \tag{19}$$

Here V is the volume of the system, e is the electric charge, $f_n^T(\boldsymbol{k},\mu)$ are the Fermi occupation functions at temperature T and chemical potential μ, and $v^i_{nm}(\boldsymbol{k})$ are the interband matrix elements of the velocity operator in the $\hat{\boldsymbol{i}}$-direction,

$$v^i_{nm}(\boldsymbol{k}) = \frac{1}{\hbar}\langle u_n(\boldsymbol{k})|\frac{\partial\hat{H}(\boldsymbol{k})}{\partial k_i}|u_m(\boldsymbol{k})\rangle, \tag{20}$$

where we have chosen the phase on the periodic part of the Bloch functions $|u_n(\boldsymbol{k})\rangle$ such that the full Bloch functions $|\Psi_n(\boldsymbol{k})\rangle = e^{i\boldsymbol{k}\cdot\hat{\boldsymbol{r}}}|u_n(\boldsymbol{k})\rangle$ are periodic in the Brillouin zone $|\Psi_n(\boldsymbol{k})\rangle = |\Psi_n(\boldsymbol{k}+\boldsymbol{G})\rangle$.

Figure 4 shows the absorption in the extreme intraorbital and interorbital dominated limits for the chemical potential in the center of the $j = 1/2$ multiplet. We consider the case of 10 electrons per unit cell such that the $j = 3/2$ multiplet is completely filled and the $j = 1/2$ multiplet is half-filled.

In the intraorbital dominated hopping regime, optical transitions between the lower and upper bands of the $j = 1/2$ multiplet near Bloch momenta surrounding the Dirac cones at the $\boldsymbol{K}$ and $\boldsymbol{K}'$ points in the Brillouin zone dominate. This feature saturates at $\hbar\omega \sim 3t_1 = \Delta^{\mathrm{intra}}_{1/2}$ where transitions between Bloch electrons at the band minima and maxima occur. The absorption vanishes for $\Delta^{\mathrm{intra}}_{1/2} < \hbar\omega < \lambda_0 - \Delta^{\mathrm{intra}}_{3/2}/2$ due to the large on-site spin-orbit coupling that splits the $j = 1/2$ and $3/2$ multiplet by a large energy gap. For $\hbar\omega > \lambda_0 - \Delta^{\mathrm{intra}}_{3/2}/2$, the conductivity vanishes due to a fine-tuned extra orbital symmetry inherited from the absence of interorbital hopping elements in the extreme intraorbital dominated coupling limit. The extra symmetry constrains the interband matrix elements of the velocity operator $\hat{\boldsymbol{v}}(\boldsymbol{k})$ to vanish between states in different multiplet sectors, forcing the conductivity to vanish at high frequencies.

In the interorbital dominated limit, the low-frequency absorption $\mathrm{Re}(\sigma(\omega))$ occurs in a narrow frequency range where light can excite particle-hole pairs within the flat bands of the $j = 1/2$ multiplet, while at higher frequencies $\hbar\omega > \lambda_0 - \Delta^{\mathrm{inter}}_{3/2}/2$ the conductivity is finite across a large range of frequencies arising from the joint density of states and the interband matrix elements of the velocity operator between the $j = 1/2$ and $3/2$ multiplet.

VII. CONCLUSION

We show that for a tight-binding model of d-orbital hopping on a honeycomb lattice, orbital frustration brought about by large on-site spin-orbit coupling and dominant intersite interorbital coupling gives rise to flat bands with bandwidths that scale as $W \sim (t_2)^2/\lambda$. Density functional theory calculations on $4d$ and $5d$ transition-metal compounds suggest that parameter regimes where t_2 dominates over t_1 are indeed viable [52]. Materials based on $5d$ transition-metal ions with larger λ and smaller U compared to the $4d$ transition-metal ions should be a particularly attractive design platform for flat band metals.

In general, *spin-orbit assisted interorbital frustration* provides a scheme for achieving flat bands in materials with a wide variety of different multiorbital structures on lattices in any dimension. In addition to quantum materials, cold atom systems have the ability to pattern intersite lattice interactions in the form of synthetic gauge potentials between multiorbital unit cells that provide a synthetic dimension providing a platform for engineering orbitally frustrated systems with flat bands in systems with a variety of lattice and multiplet on-site structures [53–57].

To achieve orbital frustration, the degrees of freedom on the lattice must be highly mixed, leading to flat bands with unique quantum geometric and topological structure described by the Berry curvature upon breaking inversion or time-reversal symmetries. Controlling orbital frustration on a lattice can lead to material design and discovery of systems on the edge of an instability toward unique correlated and topological many-body phases where the orbital structure of the ground sate plays an important role in the electronic correlations of the system. Rich phenomenology for the proposed flatband metals to show fractionalization of the electronic spectral function, nonobeyance of the Luttinger volume (Luttinger breaking), and quantized anomalous and topological Hall effects needs to be further explored.

These novel properties may then manifest in new orbital transport and orbital susceptibilities probed in the response of these systems to perturbing fields that couple to the charge and orbital degrees of freedom in the system. We hope that these material design protocols may lead to the observations and discovery of new flat band systems and new strongly correlated phases of matter defined by novel correlations in the systems' orbital degrees of freedoms.

ACKNOWLEDGMENTS

W.Z., Z.A., and N.T. acknowledge support from NSF Materials Research Science and Engineering Center Grants No. DMR-1420451 and No. DMR-2011876. Z.A. acknowledges support from the OSU President's Postdoctoral Scholars Program, which is an internal initiative sponsored by the Office of the President.

[1] M. Z. Hasan and C. L. Kane, Colloquium: topological insulators, Rev. Mod. Phys. **82**, 3045 (2010).
[2] C. L. Kane and E. J. Mele, Z2 Topological Order and the Quantum Spin Hall Effect, Phys. Rev. Lett. **95**, 146802 (2005).
[3] B. Yan and C. Felser, Topological materials: Weyl semimetals, Annu. Rev. Condens. Matter Phys. **8**, 337 (2017).
[4] B. Q. Lv, H. M. Weng, B. B. Fu, X. P. Wang, H. Miao, J. Ma, P. Richard, X. C. Huang, L. X. Zhao, G. F. Chen *et al.*, Experimental Discovery of Weyl Semimetal Taas, Phys. Rev. X **5**, 031013 (2015).
[5] X.-L. Qi and S.-C. Zhang, Topological insulators and superconductors, Rev. Mod. Phys. **83**, 1057 (2011).
[6] M. Sato and Y. Ando, Topological superconductors: a review, Rep. Prog. Phys. **80**, 076501 (2017).
[7] X. Chen, Z.-C. Gu, Z.-X. Liu, and X.-G. Wen, Symmetry protected topological orders and the group cohomology of their symmetry group, Phys. Rev. B **87**, 155114 (2013).
[8] M. Levin and X.-G. Wen, Detecting Topological Order in a Ground State Wave Function, Phys. Rev. Lett. **96**, 110405 (2006).
[9] X.-G. Wen, Topological orders in rigid states, Int. J. Mod. Phys. B **4**, 239 (1990).
[10] H. L. Stormer, D. C. Tsui, and A. C. Gossard, The fractional quantum hall effect, Rev. Mod. Phys. **71**, S298 (1999).
[11] J. Jain, Theory of the fractional quantum Hall effect, Phys. Rev. B **41**, 7653 (1990).
[12] F. D. M. Haldane, Fractional Quantization of the Hall Effect: A Hierarchy of Incompressible Quantum Fluid States, Phys. Rev. Lett. **51**, 605 (1983).
[13] X.-G. Wen, Topological orders and edge excitations in fractional quantum hall states, Adv. Phys. **44**, 405 (1995).
[14] L. Savary and L. Balents, Quantum spin liquids: a review, Rep. Prog. Phys. **80**, 016502 (2016).
[15] Y. Zhou, K. Kanoda, and T.-K. Ng, Quantum spin liquid states, Rev. Mod. Phys. **89**, 025003 (2017).
[16] A. Kitaev, Anyons in an exactly solved model and beyond, Ann. Phys. **321**, 2 (2006).
[17] D. C. Ronquillo, A. Vengal, and N. Trivedi, Signatures of magnetic-field-driven quantum phase transitions in the entanglement entropy and spin dynamics of the Kitaev honeycomb model, Phys. Rev. B **99**, 140413(R) (2019).
[18] N. D. Patel and N. Trivedi, Magnetic field-induced intermediate quantum spin liquid with a spinon fermi surface, Proc. Natl. Acad. Sci. (USA) **116**, 12199 (2019).
[19] R. L. Doretto, Plaquette valence-bond solid in the square-lattice J_1-J_2 antiferromagnet Heisenberg model: A bond operator approach, Phys. Rev. B **89**, 104415 (2014).
[20] S. Sachdev and R. N. Bhatt, Bond-operator representation of quantum spins: Mean-field theory of frustrated quantum Heisenberg antiferromagnets, Phys. Rev. B **41**, 9323 (1990).
[21] R. R. P. Singh, Z. Weihong, C. J. Hamer, and J. Oitmaa, Dimer order with striped correlations in the J_1-J_2 Heisenberg model, Phys. Rev. B **60**, 7278 (1999).
[22] V. N. Kotov, J. Oitmaa, O. P. Sushkov, and Z. Weihong, Low-energy singlet and triplet excitations in the spin-liquid phase of the two-dimensional J_1-J_2 model, Phys. Rev. B **60**, 14613 (1999).
[23] M. E. Zhitomirsky and K. Ueda, Valence-bond crystal phase of a frustrated spin-1/2 square-lattice antiferromagnet, Phys. Rev. B **54**, 9007 (1996).
[24] A. Ralko, M. Mambrini, and D. Poilblanc, Generalized quantum dimer model applied to the frustrated Heisenberg model on the square lattice: Emergence of a mixed columnar-plaquette phase, Phys. Rev. B **80**, 184427 (2009).
[25] L. Capriotti, F. Becca, A. Parola, and S. Sorella, Resonating Valence Bond Wave Functions for Strongly Frustrated Spin Systems, Phys. Rev. Lett. **87**, 097201 (2001).
[26] H.-C. Jiang, H. Yao, and L. Balents, Spin liquid ground state of the spin-$\frac{1}{2}$ square J_1-J_2 Heisenberg model, Phys. Rev. B **86**, 024424 (2012).
[27] T. Li, F. Becca, W. Hu, and S. Sorella, Gapped spin-liquid phase in the J_1-J_2 Heisenberg model by a bosonic resonating valence-bond ansatz, Phys. Rev. B **86**, 075111 (2012).
[28] J. Nasu, J. Yoshitake, and Y. Motome, Thermal Transport in the Kitaev Model, Phys. Rev. Lett. **119**, 127204 (2017).
[29] A. Pidatella, A. Metavitsiadis, and W. Brenig, Heat transport in the anisotropic Kitaev spin liquid, Phys. Rev. B **99**, 075141 (2019).
[30] P. Laurell and S. Okamoto, Dynamical and thermal magnetic properties of the kitaev spin liquid candidate α-rucl 3, npj Quantum Mater. **5**, 2 (2020).

[31] S.-H. Do, S.-Y. Park, J. Yoshitake, J. Nasu, Y. Motome, Y. S. Kwon, D. Adroja, D. Voneshen, K. Kim, T.-H. Jang *et al.*, Incarnation of majorana fermions in kitaev quantum spin lattice, arXiv:1703.01081.

[32] R. Bistritzer and A. H. MacDonald, Moiré bands in twisted double-layer graphene, Proc. Natl. Acad. Sci. (USA) **108**, 12233 (2011).

[33] J. M. B. Lopes Dos Santos, N. M. R. Peres, and A. H. Castro Neto, Continuum model of the twisted graphene bilayer, Phys. Rev. B **86**, 155449 (2012).

[34] N. N. T. Nam and M. Koshino, Lattice relaxation and energy band modulation in twisted bilayer graphene, Phys. Rev. B **96**, 075311 (2017).

[35] J. S. Hofmann, E. Berg, and D. Chowdhury, Superconductivity, pseudogap, and phase separation in topological flat bands, Phys. Rev. B **102**, 201112(R) (2020).

[36] Y. Cao, V. Fatemi, S. Fang, K. Watanabe, T. Taniguchi, E. Kaxiras, and P. Jarillo-Herrero, Unconventional superconductivity in magic-angle graphene superlattices, Nature (London) **556**, 43 (2018).

[37] Y. Cao, V. Fatemi, A. Demir, S. Fang, S. L. Tomarken, J. Y. Luo, J. D. Sanchez-Yamagishi, K. Watanabe, T. Taniguchi, E. Kaxiras *et al.*, Correlated insulator behaviour at half-filling in magic-angle graphene superlattices, Nature (London) **556**, 80 (2018).

[38] C. Xu and L. Balents, Topological Superconductivity in Twisted Multilayer Graphene, Phys. Rev. Lett. **121**, 087001 (2018).

[39] M. Ochi, M. Koshino, and K. Kuroki, Possible correlated insulating states in magic-angle twisted bilayer graphene under strongly competing interactions, Phys. Rev. B **98**, 081102(R) (2018).

[40] F. Wu, A. H. MacDonald, and I. Martin, Theory of Phonon-Mediated Superconductivity in Twisted Bilayer Graphene, Phys. Rev. Lett. **121**, 257001 (2018).

[41] Y.-H. Zhang, D. Mao, Y. Cao, P. Jarillo-Herrero, and T. Senthil, Nearly flat Chern bands in moiré superlattices, Phys. Rev. B **99**, 075127 (2019).

[42] J. M. Pizarro, M. J. Calderón, and E. Bascones, The nature of correlations in the insulating states of twisted bilayer graphene, J. Phys. Commun. **3**, 035024 (2019).

[43] J. G. Rau, E. K.-H. Lee, and H.-Y. Kee, Generic Spin Model for the Honeycomb Iridates Beyond the Kitaev Limit, Phys. Rev. Lett. **112**, 077204 (2014).

[44] J. G. Rau, Unconventional symmetry breaking in strongly correlated systems, Ph.D. thesis, University of Toronto, 2014.

[45] D. J. Griffiths and D. F. Schroeter, *Introduction to Quantum Mechanics* (Cambridge University Press, Cambridge, 2018).

[46] D. Vanderbilt, *Berry Phases in Electronic Structure Theory: Electric Polarization, Orbital Magnetization and Topological Insulators* (Cambridge University Press, Cambridge, 2018).

[47] L. Onsager, Reciprocal relations in irreversible processes. i., Phys. Rev. **37**, 405 (1931).

[48] T. Morimoto and N. Nagaosa, Nonreciprocal current from electron interactions in noncentrosymmetric crystals: roles of time-reversal symmetry and dissipation, Sci. Rep. **8**, 2973 (2018).

[49] F. G. Utermohlen and N. Trivedi, Symmetry analysis of tensors in the honeycomb lattice of edge-sharing octahedra, Phys. Rev. B **103**, 155124 (2021).

[50] J. E. Sipe and E. Ghahramani, Nonlinear optical response of semiconductors in the independent-particle approximation, Phys. Rev. B **48**, 11705 (1993).

[51] D. J. Passos, G. B. Ventura, J. M. V. Parente Lopes, J. L. dos Santos, and N. M. R. Peres, Nonlinear optical responses of crystalline systems: Results from a velocity gauge analysis, Phys. Rev. B **97**, 235446 (2018).

[52] H.-S. Kim and H.-Y. Kee, Crystal structure and magnetism in α- rucl 3: An ab initio study, Phys. Rev. B **93**, 155143 (2016).

[53] N. Goldman, G. Juzeliūnas, P. Öhberg, and I. B. Spielman, Light-induced gauge fields for ultracold atoms, Rep. Prog. Phys. **77**, 126401 (2014).

[54] Y.-J. Lin and I. Spielman, Synthetic gauge potentials for ultracold neutral atoms, J. Phys. B **49**, 183001 (2016).

[55] A. Celi, P. Massignan, J. Ruseckas, N. Goldman, I. B. Spielman, G. Juzeliūnas, and M. Lewenstein, Synthetic Gauge Fields in Synthetic Dimensions, Phys. Rev. Lett. **112**, 043001 (2014).

[56] K. Jiménez-García, L. J. LeBlanc, R. A. Williams, M. C. Beeler, C. Qu, M. Gong, C. Zhang, and I. B. Spielman, Tunable Spin-Orbit Coupling Via Strong Driving in Ultracold-Atom Systems, Phys. Rev. Lett. **114**, 125301 (2015).

[57] N. R. Cooper, J. Dalibard, and I. B. Spielman, Topological bands for ultracold atoms, Rev. Mod. Phys. **91**, 015005 (2019).